Electronic structure and scanning tunneling microscopy images of heterostructures consisting of graphene and carbon-doped hexagonal boron nitride layers

Taishi Haga [1,*] Yoshitaka Fujimoto,[1] and Susumu Saito[1,2,3]

[1]*Department of Physics, Tokyo Institute of Technology, 2-12-1 Oh-okayama, Meguro-ku, Tokyo 152-8551, Japan*

[2]*Advanced Research Center for Quantum Physics and Nanoscience, Tokyo Institute of Technology, 2-12-1 Oh-okayama, Meguro-ku, Tokyo 152-8551, Japan*

[3]*Materials Research Center for Element Strategy, Tokyo Institute of Technology, 4259 Nagatsuta-cho, Midori-ku, Yokohama, Kanagawa 226-8503, Japan*

We perform first-principles total-energy calculations within the framework of the density-functional theory to investigate electronic properties of graphene/C-doped hexagonal boron nitride (*h*-BN) heterostructures. We consider both the monolayer *h*-BN case and the trilayer *h*-BN case. From the electronic-structure analysis, it is found that substitutional doping of the C atom at the B site and that at the N site in underlying *h*-BN lead to asymmetric charge carrier concentrations in the graphene layer, indicating the importance of the impurity atom in the *h*-BN substrate and its polarity in the electronic transport properties of graphene/*h*-BN heterostructures. We also find that simulated scanning tunneling microscopy (STM) images of the graphene surface on the C-doped *h*-BN layer at the B site and that at the N site are considerably different from each other in both monolayer and trilayer *h*-BN cases. While the B site doping of the C atom in *h*-BN substrate layers essentially does not change the STM image of the graphene surface on the pristine *h*-BN, the C atom doped at the N site considerably modifies the STM image of graphene even in the case of the doping in the third layer of the trilayer *h*-BN. Therefore, when the graphene in used as a cover layer to the *h*-BN layered materials and thin films, the STM should be a useful tool to detect the acceptor C atoms in the *h*-BN not only at the topmost surface layer but also at second and third layers. We clarify the origin of these characteristic features of the STM images in terms of spatial distributions of the local density of states induced by the dopant C atom.

I. INTRODUCTION

Two-dimensional (2D) layered materials including graphene and hexagonal boron nitride (*h*-BN) layers are attracting much attention since they possess remarkable properties, e.g., high carrier mobility of graphene [1–3] and high thermal conductivity of *h*-BN [4–6] due to their unique electronic and mechanical properties. Furthermore, by constructing stacked-layer heterostructures with various types of 2D atomic layers, new and controllable physical properties should emerge [7–10]. Like graphene, *h*-BN has a honeycomb lattice structure consisting of alternating boron and nitrogen atoms, and is often called white graphite due to its similar mechanical properties and the color of *h*-BN. It is well known that *h*-BN is a wide-gap semiconductor with the fundamental gap of about 6 eV, being different from metallic graphene [11–13]. It has been reported that *h*-BN is a good substrate for graphene compared with a conventional SiO_2 substrate [14–18] because of the absence of dangling bonds, an atomically flat geometry, and a small lattice mismatch (about 1.8%) [19,20]. Nonetheless, according to the recent scanning tunneling microscopy (STM) study of monolayer graphene stacked onto *h*-BN substrates, there should be

intrinsic defects in underlying *h*-BN [21]. The STM is known to be a powerful tool to detect and identify defects in atomic layer materials, especially when combined with the first-principles electronic-structure study. Therefore, these defects in graphene/*h*-BN heterostructures must be further studied both theoretically and experimentally because defects in semiconductors often play a crucial role in determining the electronic transport properties of the system. Actually, it has been suggested that defects in *h*-BN substrates affect transport properties of graphene [21]. It has been also demonstrated experimentally that carbon atoms as well as oxygen atoms are incorporated into the hexagonal network of *h*-BN atomic layers during synthesis of *h*-BN [22–25]. Theoretically, there have been studies on effects of impurities in *h*-BN, including carbon and oxygen defects as well as atomic vacancies [26–28]. For example, carbon impurity states are suggested to appear within the fundamental gap of *h*-BN atomic layers and those impurity states are shown to be relatively deep [29,30]. Although several theoretical studies on the impurities in the *h*-BN atomic layers have been reported so far, there are few theoretical reports on effects of the impurities on the electronic properties of graphene stacked onto *h*-BN substrates when the impurities are present in the underlying *h*-BN.

In this paper, using first-principles electronic-structure calculations, we study how the electronic properties of the

*haga.t@stat.phys.titech.ac.jp

graphene/*h*-BN heterostructures change when a C atom is doped in underlying *h*-BN layers, and how the change will be detected in the STM measurement. We discuss the detailed geometries of heterostructures composed of the graphene monolayer on the doped as well as pristine *h*-BN layers. We also show the energy band structures of these heterostructures doped with C atoms in the *h*-BN layers. It is found that the substitutional doping of the C atoms at B and N sites in underlying *h*-BN layers gives rise to asymmetric charge carrier densities on the graphene layer. The STM images of the graphene on C-doped *h*-BN substrates are simulated, and the STM images of graphene/*h*-BN heterostructures doped with C atoms at the B site and N site are found to be considerably different from each other. We find that, while the C impurities at B sites in *h*-BN substrate layers essentially does not change the STM image of graphene, the C impurities at N sites affect electronic states of the system up to the surface graphene layer, and they can be visualized even in the case of the C impurities in the third *h*-BN layer by using STM observations over the graphene surface. Therefore, the STM should be a powerful tool to detect C impurities in the substrate *h*-BN layers in the graphene/*h*-BN heterostructures.

This paper is organized as follows. In Sec. II, the computational methods used in the present paper are introduced, and the geometries of the graphene/*h*-BN heterostructures considered are explained in detail. In Sec. III, optimized geometries and electronic structures of graphene/*h*-BN heterostructures with pristine and doped *h*-BN layers are reported, and the simulated STM images are discussed. The summary of the paper is given in Sec. IV.

II. COMPUTATIONAL METHODS AND SYSTEMS STUDIED

A. Computational methods

We perform first-principles total-energy calculations by using the local density approximation (LDA) within the framework of the density-functional theory (DFT) [31–34]. The interactions between the ions and the valence electrons are described by the Vanderbilt ultrasoft pseudopotentials [35]. It has been reported that the LDA calculations give comparable results with generalized gradient approximation (GGA) calculations including van der Waals (vdW) interactions for relative energies and interlayer distances of multilayered materials such as the *h*-BN bulk, graphite, and graphene/*h*-BN heterostructures [36–40]. Nonetheless, to compare further the results of LDA and GGA + vdW calculations, we have also performed GGA + vdW calculations in two-layer systems [41–43]. The cutoff energies of a plane-wave basis and a charge density are taken to be 35 Ry and 350 Ry, respectively. We use 6×6 supercells having 144 atoms and 288 atoms for the two-layer system and the four-layer system, respectively. This supercell size should be large enough to deal with relatively localized substitutional C-impurity states in *h*-BN layers [30]. We also study a C-doped rotated two-layer system with the supercell of 112 atoms to discuss the incommensurate stacking effect as will be explained in the next subsection. The supercell length along the direction perpendicular to 2D layers is taken to be enough long and the interlayer distance

between the top and the bottom layer in the neighboring supercells is kept to the longer than 20 Å in all the cases studied. For the Brillouin-zone integration, $6 \times 6 \times 1$ *k*-point sampling is used for the C-doped two-layer and four-layer systems, while $8 \times 8 \times 1$ *k*-point sampling is used for the C-doped rotated two-layer system. We have confirmed the convergence of these *k*-point samplings by comparing results using the $6 \times 6 \times 1$ *k*-point sampling with those using the $8 \times 8 \times 1$ *k*-point sampling, and those using the $8 \times 8 \times 1$ *k*-point sampling with those using the $10 \times 10 \times 1$ *k*-point sampling. Geometries of all the systems studied are fully optimized until Hellmann-Feynman forces acting on all atoms become less than 0.005 eV/Å. All calculations are performed using the Quantum ESPRESSO package [44].

To discuss the energetics, we define the formation energy E_f:

$$E_f = (E_{\text{tot}} - E_{\text{gra}} - mE_{h-\text{BN}})/N. \tag{1}$$

Here E_{tot}, E_{gra}, and $E_{h-\text{BN}}$ are total energies of the graphene/*h*-BN heterostructures, the graphene monolayer, and the *h*-BN monolayer, respectively, *m* is the number of *h*-BN layers of the graphene/*h*-BN heterostructures, and *N* is the number of atoms in the supercell.

The simulated STM images are obtained based on the Tersoff-Hamann approximation [45]. Within this approximation, the tunneling current *I* at **r** under an applied bias voltage *V* is proportional to the integration of the local density of states (LDOS) over the energy range from E_F to $E_F + \text{eV}$:

$$I(\mathbf{r}) \sim \int_{E_F}^{E_F+\text{eV}} \rho(\mathbf{r}, E) dE, \tag{2}$$

where $\rho(\mathbf{r}, E) = \Sigma_i |\Psi_i(\mathbf{r})|^2 \delta(E - E_i)$ and E_F is the Fermi energy. The negative and positive bias voltage reflect the occupied and unoccupied electronic states, respectively. We refer to this "energy-integrated LDOS" as EI-LDOS [46–48], which is a useful theoretical viewgraph to investigate the impurity effect for not only the surface region but also the region under the surface atomic layers as will be shown later. We use VESTA package to draw the STM images [49]. All the STM images reported in the present paper are for the constant-height modes with the height of 2 Å. The STM images simulated using the above procedure for defects in atomic layers have been confirmed to be highly accurate. The STM image of the substitutional N impurity in the graphene monolayer was predicted to have three bright spots corresponding to the three nearest-neighbor C atoms around the N impurity [50]. The STM measurement later confirmed the presence of three bright spots in this system [51]. We therefore expect the high reliability of the simulated STM images given in the present paper.

B. Geometries studied

We consider four types of two-layer systems composed of the *h*-BN monolayer and the graphene monolayer, and a four-layer system composed of *h*-BN trilayer and the graphene monolayer as schematically shown in Figs. 1(a)–1(d) and Fig. 1(e), respectively. In the two-layer systems, we consider four different stacking patterns: *Aa*, *Ab*, Ab′, and rotated
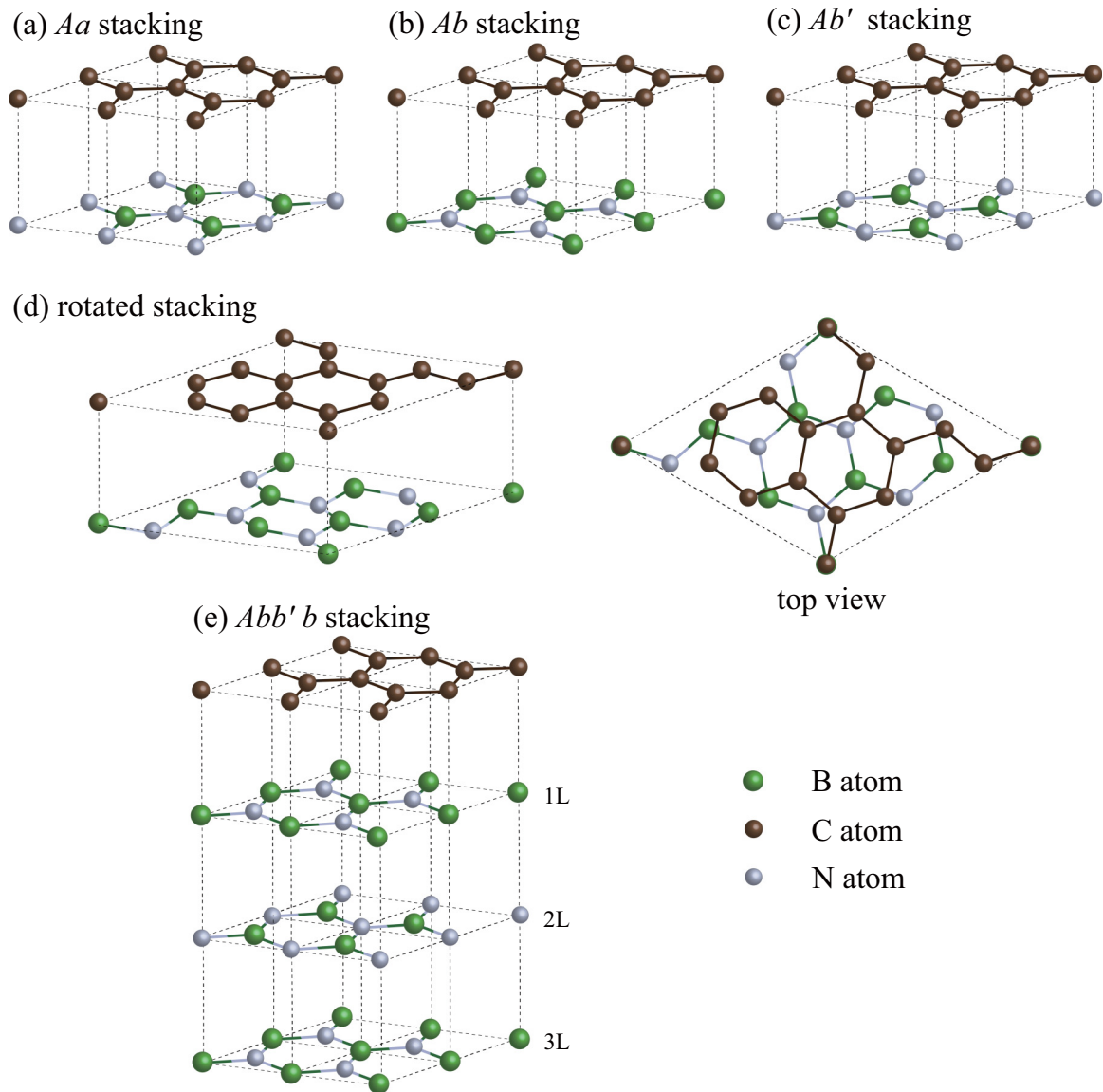
FIG. 1. Atomic geometries of four kinds of two-layer systems with (a) *Aa*, (b) *Ab*, (c) *Ab′*, and (d) rotated stackings, and (e) that of a four-layer system with *Abb′b* stacking. In the *b′* *h*-BN layer, B atoms are placed at the N atom sites of the *b* layer, and vice versa. In the rotated two-layer system, the rotated graphene with an angle of 21.8° is placed on the *h*-BN monolayer. In the four-layer system, graphene monolayer is stacked on the *h*-BN trilayer consisting of 1L, 2L, and 3L (see text). Dotted lines are guides to the eye to indicate the unit cell.

stackings. In the present paper, all the geometrical parameters including lattice constants of the hexagonal cell are optimized in each case. Since we assume the commensurate case, the graphene layer is found to expand slightly and the *h*-BN layer is compressed upon the optimization as will be discussed later in detail. For the *Aa* stacking shown in Fig. 1(a), C atoms in the graphene layer are placed on top of both B and N atoms in the *h*-BN layer. For the *Ab* stacking shown in Fig. 1(b), one of the two C atoms in a unit cell in the graphene layer is above the B atom while the other C atom is on top of the center of a hexagon of the *h*-BN layer. For the *Ab′* stacking shown in Fig. 1(c), one of the two C atoms is on top of the N atom and the other is above the center of a hexagon of the *h*-BN layer. It should be noted that the nomenclature of the preceding paper [7] is used for the stacking patterns. Therefore, the capital letter (*A*) indicates the relative position of the graphene

layer, and the small letters (*a*, *b*, and *b′*) indicate the relative positions and the relative directions of the *h*-BN layers. For the rotated system shown in Fig. 1(d), the rotated graphene with the angle of 21.8° is stacked on the *h*-BN monolayer and the unit cell of the rotated system has 14 C atoms in the graphene layer and seven B atoms and seven N atoms in the *h*-BN monolayer. We consider this rotated system to simulate the interactions between the graphene and *h*-BN layers with incommensurate stacking. It is known that the *aa′* stacking pattern is often observed in the *h*-BN bulk [52,53]. Hence, for the four-layer heterostructure shown in Fig. 1(e), the graphene monolayer is stacked on the trilayer *h*-BN with the stacking pattern equivalent to the *aa′* pattern [54].

We next consider graphene/C-doped *h*-BN heterostrctures. In the *h*-BN layer, there are two kinds of substitution sites for C-atom doping, B and N sites, and the C atom substitutionally
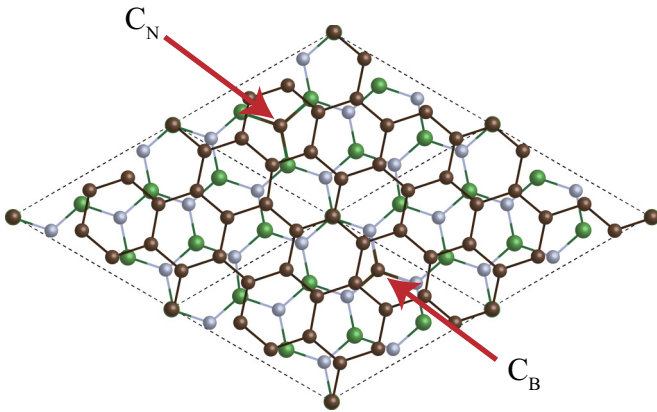
FIG. 2. Top view of atomic structure of C-doped rotated two-layer system with 2×2 supercell having 112 atoms. The C substitution sites of B atom and N atom nearly under the center of hexagon of the graphene layer are indicated by arrows with C_B and C_N, respectively. The dotted line denotes the unit cell of the pristine phase.

doped in these sites are named as C_B and C_N, respectively. In the Aa stacked two-layer system, the C atom doped at the B site or N site in the h-BN layer is located directly below the C atom in the graphene layer. In the Ab stacked two-layer system, the C atom doped at the B site in the h-BN layer is just below the C atom in the graphene layer, while the C atom doped at the N site is below the center of the hexagon of the graphene layer. In the case of the rotated two-layer system shown in Fig. 1(d), there are seven different substitution sites for C atom doping, both at the B site and at the N site. In the present paper, we have studied the C doping at two kinds of B sites and also two kinds of N sites among seven sites in each case. However, the doping-site dependence of the band structure as well as that of the STM image is found to be very small, and we will show the results for the C doping at B and N sites in the h-BN layer which are nearly below the center of the hexagon of the graphene layer as shown in Fig. 2.

In the C-doped four-layer system, we treat only the C atom dopings at the N site. Thereby, the C_N atom is positioned below the center of the hexagon of the graphene layer when C atom is doped into the top layer (1L) or the bottom layer (3L) in the h-BN trilayer, while the C_N atom is below the C atom of the graphene layer when the C_N atom is doped into the middle layer (2L).

III. RESULTS AND DISCUSSION

A. Atomic structures and energetics

We first show the structural properties and the energetics for optimized atomic structures of the undoped graphene/h-BN two-layer and four-layer systems. In Table I, we list total energies and interlayer distances between graphene and h-BN layers. The optimized in-plane lattice constants for the two-layer systems with three stacking patterns are found to be identical, 2.468 Å, corresponding to the average value of optimized lattice constants of the graphene monolayer (2.446 Å) and the h-BN monolayer (2.490 Å), obtained using the same methodology. In the rotated two-layer system, the optimized in-plane lattice constant is 6.530 Å,

TABLE I. Interlayer distances and formation energies of two-layer and four-layer systems for graphene/h-BN heterostructures. For the four-layer system, the interlayer distance between graphene and the top layer of the h-BN (1L) is listed.

System	Stacking pattern	Interlayer distance (Å)	Formation energy (meV/atom)
Two-layer	Aa	3.52	-0.21
	Ab	3.23	-5.65
	Ab'	3.46	-1.03
	Rotated	3.39	-4.77
Four-layer	$Abb'b$	3.22	-9.26

which corresponds to the average $B - N$ ($C - C$) distance of 1.425 Å, the same as that of other three two-layer systems. For the four-layer system, the optimized in-plane lattice constant is 2.479 Å. Thus, our calculated in-plane lattice constants of the graphene/h-BN heterostructures are in good accord with experimental values [55,56] and calculated results [37,50,57–59] for graphene and for h-BN.

From Table I, we find that the Ab stacking is the most stable stacking pattern with the shortest interlayer distance (3.23 Å) among the four types of two-layer systems studied. It should be notated that none of these two-layer systems possesses the perfectly flat h-BN layer, and indeed the presence of up-down shift with the order of 0.001 Å is observed. The rotated system is the second stable structure with the energy difference of only 0.88 meV/atom while the interlayer distance is considerably longer than that of the Ab stacking. The Ab' stacking is the third stable structure and its total energy is much higher by 4.62 meV/atom compared with that of the Ab stacking. The energy difference between the Ab and the Ab' stackings would be attributed to the interlayer interactions: The interaction between the B atom in the h-BN layer and the C atom in graphene layer is more favorable in energy than that between the N atom and the C atom. This behavior was reported in previous theoretical studies [7,60]. In the case of the rotated two-layer system, not only the $B - C$ type interlayer interaction but also the $B - N$ type interlayer interaction is present, as shown in Fig. 2. Therefore, the rotated system is slightly less stable than the Ab stacking structure. In the case of the four-layer system, the optimized interlayer distance between graphene and the top layer of h-BN is 3.22 Å, whereas the interlayer distances between the neighboring layers of the h-BN trilayer are both 3.24 Å. The four-layer system takes considerably lower formation energy compared with the Ab-stacked two-layer systems since two more sets of interlayer interactions among the trilayer of the h-BN give rise to the sizable energy gain.

We now show the structural properties of the two-layer heterostructures of C-doped h-BN at the B site and graphene. We first examine the detailed structures around the impurity C atom doped at the B site of the h-BN layer. The optimized in-plane bond lengths between the C atom and the neighboring N atoms for the C-doped two-layer systems with Aa, Ab, and Ab' stackings as well as for the rotated two-layer system are almost identical, 1.36 Å. This in-plane $C - N$ bond length is considerably shorter than the $B - N$ bond length for the undoped graphene/h-BN heterostructures. These impurity C

atoms doped at the B site in the heterostructure nearly reside in the host *h*-BN plane as in the case of the C atom doped at the B site of the *h*-BN monolayer [30].

We next examine the structural properties of the two-layer heterostructures of C-doped *h*-BN at the N site. The optimized in-plane bond lengths between the impurity C atom in the *h*-BN layer and the neighboring B atoms for the C-doped two-layer systems with the *Aa*, *Ab*, and *Ab'* stackings and for the rotated two-layer system are again almost identical, 1.47 Å. However, the C_N atom is found to no longer be on the host *h*-BN plane. In the case of the *Aa*-stacked and *Ab'*-stacked two-layer systems, the C_N atom protrudes by 0.62 Å and 0.59 Å, respectively, from the *h*-BN planar layer toward the graphene layer, whereas the C_N atom moves also toward the graphene layer by only 0.05 Å for the *Ab*-stacked two-layer system. These structural deformations may indicate the presence of the attractive interaction between the impurity C atom in the *h*-BN layer and the C atom in the neighboring graphene layer as will be discussed in the following. For the *Aa* and *Ab'* stackings, the impurity C atom in the *h*-BN layer is located directly below the C atom in graphene, while for the *Ab* stacking, it is located below the center of the hexagon of graphene. In the case of the rotated two-layer system, the impurity C atom in the *h*-BN layer also moves toward the graphene layer by 0.08 Å. This is reasonable since, in this case, the C_N is located not directly below the hexagon center site of the graphene layer but rather close to there. In the case of four-layer heterostructures, we have examined the C doping at N sites. The optimized in-plane $B - C$ bond lengths are found to always be 1.48 Å. On the other hand, the impurity C atom resides in the *h*-BN planar layer, irrespective of the depth of the doped *h*-BN layer from the top graphene layer. It should be noted that it has been reported that the substitutional doping with a C atom in the *h*-BN monolayer at the B site is energetically favorable rather than that at the N site [30].

In the GGA + vdW calculations, in-plane lattice constants of two-layer systems composed of graphene and *h*-BN monolayer are 2.488 Å, and interlayer distances are found to be 3.38 Å, 3.14 Å, and 3.32 Å for the *Aa*, *Ab*, and *Ab'* stacking,

respectively. Interestingly, formation energies are found to be rather large −17.7, −25.4, −20.5 meV/atom for the *Aa*, *Ab*, and *Ab'*, respectively. In-plane lattice constants are longer and interlayer distances are shorter than those given by the LDA calculations. These geometrical differences are found to give a slight change of the depth of the impurity-induced state measured from the Dirac-cone apex in the graphene/*h*-BN with C_N: the depth by GGA + vdW is 0.302 eV while that by the LDA is 0.350 eV. If we use the LDA geometry for the GGA + vdW band-structure calculation, the depth is 0.344 eV, being very close to the LDA value. On the other hand, the difference of 0.048 eV in the depth of the impurity-induced state in the LDA and in the GGA + vdW is found to give negligible difference in the STM images, which are confirmed to be almost identical with each other. To study further the nature of the interaction between the impurity C atom and the C atom in the neighboring graphene layer, structural deformations in the C-doped two-layer systems are also obtained using GGA + vdW calculations. In the GGA + vdW calculations, the C_N atom protrudes by 0.48 Å and 0.43 Å for the *Aa* and *Ab'* stacking, respectively. These values of protrusion are actually smaller than those of LDA, indicating that the attractive interaction between the impurity C atom at the N site and the graphene C atom is not the vdW type but some chemical interaction. Furthermore, in the calculations of the C-doped *h*-BN single layer without the graphene layer, the dopant C atom remains in the planar *h*-BN layer. Underestimation of the interlayer distances in the GGA + vdW may be the origin of the reduction of the protrusion of the impurity C atom. Importantly, the interlayer distances of graphite and bulk *h*-BN given by the GGA + vdW (3.22 Å and 3.11 Å) are both known to be shorter than the experimented values [61,62] (3.34 Å and 3.33 Å), while those given by the LDA (3.32 Å and 3.24 Å) are much closer to the experimental values. In the following, therefore, we will show the results obtained by LDA.

B. Energy band structures

We study energy band structures of the *Ab*-stacked two-layer system, the rotated two-layer system, and the four-layer
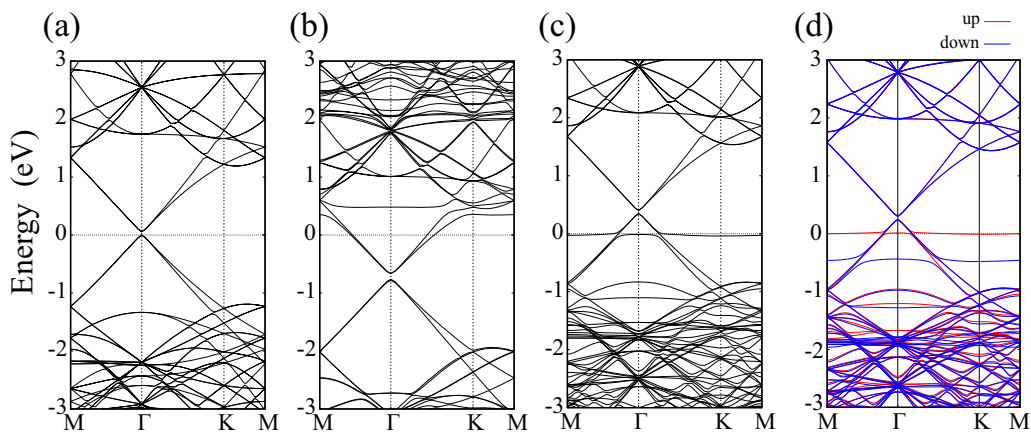
FIG. 3. Energy band structures of the *Ab*-stacked graphene/*h*-BN two-layer systems. (a) Pristine *h*-BN case, (b) C-doped *h*-BN at the B site case, and (c) and (d) that at the N site case. The Fermi level is set to zero. The 6×6 supercell is used not only for the band structure of doped cases but also for that of the pristine case. Band structures are obtained by using the LDA calculation in (a)–(c) and the LSDA calculation in (d).
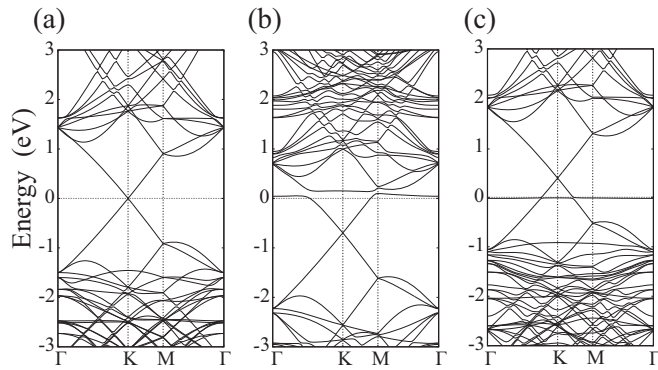
FIG. 4. Energy band structures of the rotated graphene/*h*-BN two-layer system. (a) Pristine *h*-BN case, (b) C-doped *h*-BN at the B site case, and (c) that at the N site case. The Fermi level is set to zero. The 2 × 2 supercell is used not only for the band structure of doped case but also for that of the pristine case.

FIG. 5. Energy band structures near the Fermi level of four-layer systems doped with C atom at the N site in (a) top layer (1L), (b) middle layer (2L), and (c) bottom layer (3L) of *h*-BN trilayer. The Fermi level is set to zero.

system. Figure 3 shows energy band structures of the *Ab*-stacked two-layer systems. In the pristine *Ab*-stacked two-layer system, the finite band gap opens at the apex of the Dirac cone at the Γ point and its value is 0.06 eV, shown in Fig. 3(a), since the sublattice symmetry of the C atoms of graphene is broken due to the interlayer interactions with the *h*-BN layer. When a C atom is doped at the B site and the N site in the underlying *h*-BN layer, the donorlike and the acceptorlike states appear near the Fermi level as shown in Figs. 3(b) and 3(c), respectively. These results are in agreement with theoretical studies reported previously [63]. In the B site doped case as shown in Fig. 3(b), a nearly flat band appears around 0.5 eV above Fermi level. Therefore, the electron originally at this donorlike state is now completely transferred to the graphene, which now has an electron carrier. In the case of the N site doping as shown in Fig. 3(c), on the other hand, a nearly flat band appears just around the Fermi level, and the transfer of the hole from this acceptorlike state to the graphene is found to take place only partially.

We have also performed the spin-polarized density-functional calculations using the local spin density approximation (LSDA) for the C-doped graphene/*h*-BN heterostructures. The C-doped graphene/*h*-BN heterostructures with the *Ab* stacking for the B-site doping is found to be nonmagnetic, while total magnetization for the N-site doping is 0.88 Bohr mag/cell. Figure 3(d) shows the LSDA energy band structure of the *Ab*-stacked two-layer system with the C_N. As in the case of LDA calculation, the acceptor state appears near the Fermi level. As will be shown later, this spin polarization essentially does not affect the STM images.

In Fig. 4, we show the energy band structures of the rotated two-layer systems. The undoped rotated two-layer system possesses almost zero band gap, shown in Fig. 4(a). When the C atom is doped into the rotated system at the B site and the N site, the donorlike and the acceptorlike states, respectively, also appear near the Fermi level as shown in Figs. 4(b) and 4(c). Interestingly, for the rotated two-layer system, the donorlike state is located slightly above the Fermi level and the electron transfer from the state to graphene is complete as in the case of the *Ab*-stacked two-layer system. The acceptorlike state in the C_N-doped case appears again just
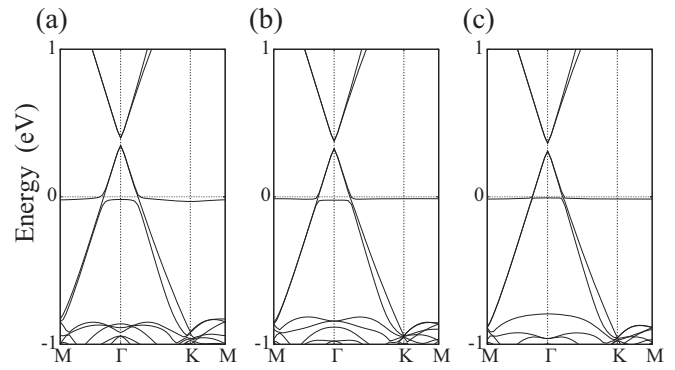
at the Fermi level as shown in Fig. 4(c). Therefore, the hole transfer is incomplete and the Dirac cone apex is relatively close to the Fermi level as in the case of the *Ab*-stacked two-layer system. Thus, the substitution of the B or the N atom with the C atom in underlying *h*-BN can produce asymmetric charge carrier densities on graphene layers.

We also study energy band structures of the C-doped four-layer systems. Figures 5(a)–5(c) show the energy-band structures near the Fermi level of the graphene stacked on the C-doped *h*-BN trilayers at the N site, where the C atom is doped to the top layer (1L), the middle layer (2L), and the bottom layer (3L) in the *h*-BN trilayer, respectively [see Fig. 1(e)]. It is found that the acceptorlike states are induced near the Fermi level and the depth of the Fermi level from the Dirac cone apex is almost independent of the C-doped *h*-BN layer number. Therefore, the hole concentration on the graphene layer should be the same in three cases. On the other hand, it is also found that the acceptorlike states change from dispersive to flat bands as the doped *h*-BN layer goes away from the graphene layer. Thus, as the distance between the graphene layer and the doped *h*-BN layer increases, the interlayer interaction between the acceptorlike state induced by the C-doped *h*-BN layer and π-orbital states of the graphene decreases, which gives rise to peculiar STM images depending on the doped *h*-BN layer number, as will be discussed in the next subsection.

In the present paper, the 6 × 6 supercell is used with the plane-wave basis set. Both the donor state and the acceptor state are found to have very small dispersions and can be identified rather easily, confirming that the supercell used is large enough. The depth of the acceptor state, on the other hand, should depend on the supercell size because the state appears just at the Fermi level. For lower-density doping case, the electron transfer from graphene to the acceptor state is less, and the Fermi level should be higher. Consequently, the acceptor state would be higher in energy as well. To check the convergence of its depth, a huge supercell might be necessary with the identification method of the C_N-origin state in the tiny Brillouin zone. The localized-basis calculation with unfolding method [64] would therefore be an interesting future study.
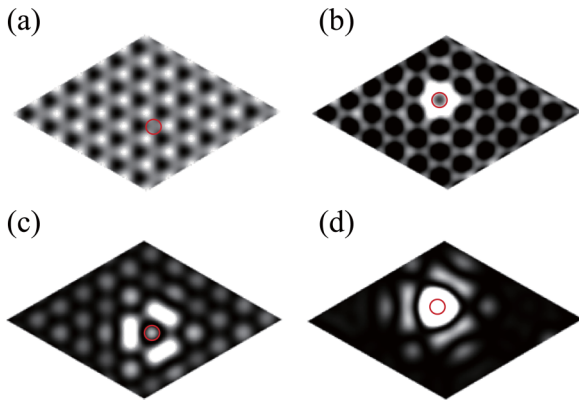
FIG. 6. Simulated STM images of the *Ab*-stacked two-layer system to be taken over the graphene layer with (a) C_B and (b) C_N, and these to be taken under the *h*-BN layer with (c) C_B and (d) C_N. The STM images are constructed at applied bias voltages of $+0.5$ eV for (a) and (c), and -0.5 eV for (b) and (d). The red circle in each figure denotes the position of the C atom doped in the *h*-BN layer.

C. Scanning tunneling microscopy

We study STM images of the graphene/C-doped *h*-BN two-layer systems with various stacking patterns. Figures 6(a) and 6(b), respectively, show the STM images on the constant-height plane over the graphene layer on top of the C-doped *h*-BN layer at the B site and the N site for the *Ab*-stacked two-layer. In the B site doped case, the impurity-induced state is located at about 0.5 eV higher than the Fermi level as discussed above. Hence, we simulate the STM image with the bias voltage of $+0.5$ eV. In the N site doped case, on the other hand, we use the bias voltage of -0.5 eV. In the STM images over the graphene layer on the *h*-BN layer with C_B, there are large bright spots arranged perfectly on the hexagonal lattice points as if the C-impurity were absent in the underlying *h*-BN layer [Fig. 6(a)]. These blight spots are located just above C atoms, which are on top of the hexagon center of the underlying *h*-BN layer. The other-type C atom, which is on top of the B atom of the *h*-BN layer, is only weakly bright while the hexagon center of the graphene layer itself corresponds to the dark area of the image. The impurity site does not show up clearly because the STM image mainly reflects π^*-orbital states of graphene and these states are not affected by C_B as will be shown later. Interestingly, the STM image over the graphene layer on the *h*-BN with C_N exhibits a sharp contrast to that with C_B. There appears a hexagon-shaped bright area above the impurity C atom with three brighter C atoms on top of B atoms in the underlying *h*-BN. Thus, it is interesting that the C_N impurity in the *h*-BN layer is clearly visible in the heterostructure with graphene by the STM method, whereas C_B is not.

The C_B impurity in the *Ab* stacked two-layer system can be observed in the STM measurement if it is taken from the *h*-BN layer side. Figures 6(c) and 6(d), respectively, show the STM images over the constant-distance plane below the C-doped *h*-BN layer at the B site and the N site for the *Ab*-stacked two-layer. In the STM image of the B-site doped case, there is a small bright spot below the C-atom impurity surrounded by three of bright heavy lines connecting two B atoms. On
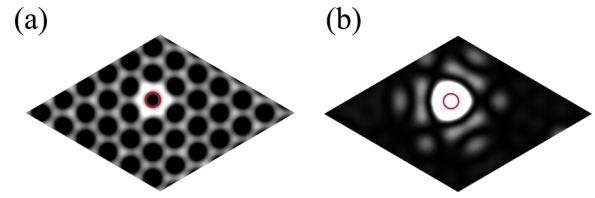
FIG. 7. Simulated STM images of the *Ab*-stacked two-layer system to be taken (a) over the graphene layer and (b) below the *h*-BN layer with C_N. These STM images are constructed at applied bias voltages of -0.5 eV. These STM images have been obtained by using the LSDA calculation. The red circle in each figure denotes the position of the C atom doped in the *h*-BN layer.

the other hand, in the STM image of the N-site doped case, there exists a large triangle-shaped bright area surrounded by three bright fine lines connecting two N atoms. This image is consistent with the C impurity state having the triangular spatial distributions of the LDOS to be shown later. These results are in good accord with our previous study on C-doped *h*-BN monolayers [30].

We also study STM images by using the LSDA calculation. Figures 7(a) and 7(b), respectively, show the STM images on the constant-height plane over the graphene layer and below the *h*-BN layer. These STM images are almost identical to those of Figs. 6(b) and 6(d) obtained using the LDA. Since it is confirmed that the LDA is sufficient for simulating the STM image, in the following we will show only the results obtained by using the LDA.

Figures 8(a)–8(c) show the STM images on the constant-height plane over the graphene layer on C-doped *h*-BN at the N site for the *Aa*-stacked, *Ab'*-stacked, and the rotated two-layer system, respectively. Interestingly, as in the case of the *Ab*-stacked two-layer system, the STM image of the rotated two-layer system has a hexagon-shaped bright area, while that of the *Aa*-stacked two-layer system has a triangle-shaped bright area. We can now expect that in the two-layer system with any stacking pattern, C_N impurities in the *h*-BN can be observed by the STM over the graphene layer.
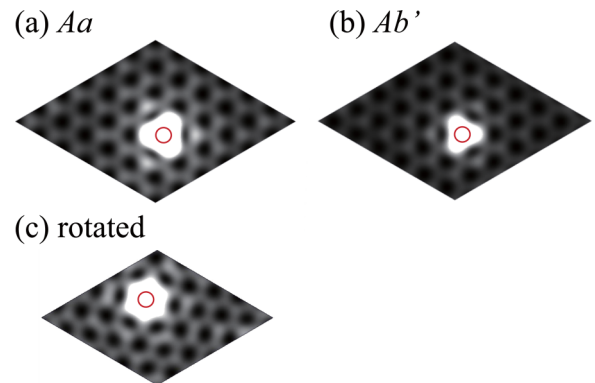
FIG. 8. Simulated STM images of graphene layer on C-doped *h*-BN at N site for the (a) *Aa*-stacked, (b) *Ab'*-stacked, and (c) rotated two-layer system. The STM images are constructed at applied bias voltage of -0.5 eV for all three cases. The red circle in each figure denotes the position of the C atom doped in the *h*-BN layer.
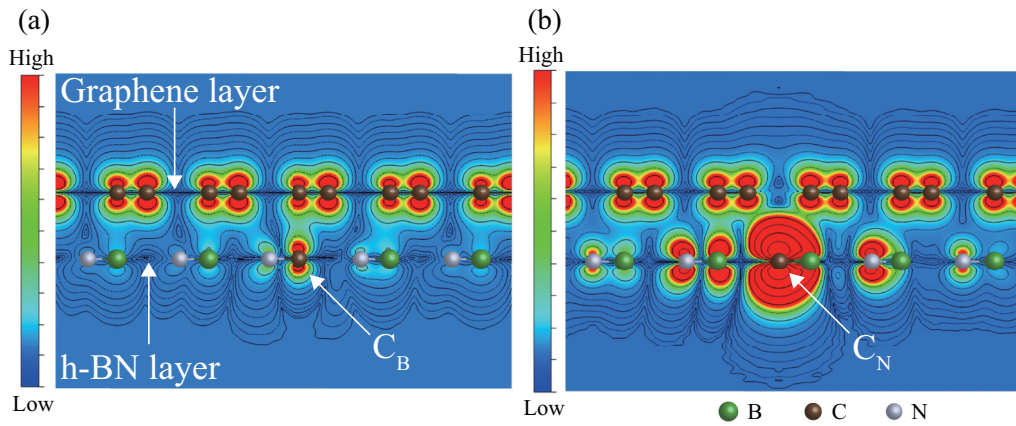
FIG. 9. Contour maps of EI-LDOS of graphene/C-doped h-BN at (a) B site and (b) N site for Ab-stacked two-layer systems. The LDOS are integrated from E_F to $E_F + 0.5$ eV in (a) and $E_F - 0.5$ eV to E_F in (b). Contour lines are drawn in logarithmic scales.

Let us analyze here how the acceptor states induced by the C-atom impurity in the underlying h-BN affect the STM images over the graphene layer stacked on the C-doped h-BN layer. Figures 9(a) and 9(b) show cross sections of contour plots of the EI-LDOS of graphene/C-doped h-BN at the B site and that at the N site for the Ab-stacked two-layer system, respectively. In the case of the C-doped h-BN at the B site, the modulated area of EI-LDOS around the C impurity spatially are localized, and therefore those above the graphene layer are

almost unchanged, as shown in Fig. 9(a). On the other hand, the spatial distributions of the EI-LDOS around the C impurity in the h-BN layer doped at the N site are considerably modified, indicating the extension of the impurity induced state above and below the h-BN layer. It therefore affects the shape of the topmost contour line of Fig. 9(b), which gives rise to the bright area in the STM image. These differences in the spatial distributions of the C_B- and C_N-induced states may arise from the size differences between B, C, and N atoms. When the
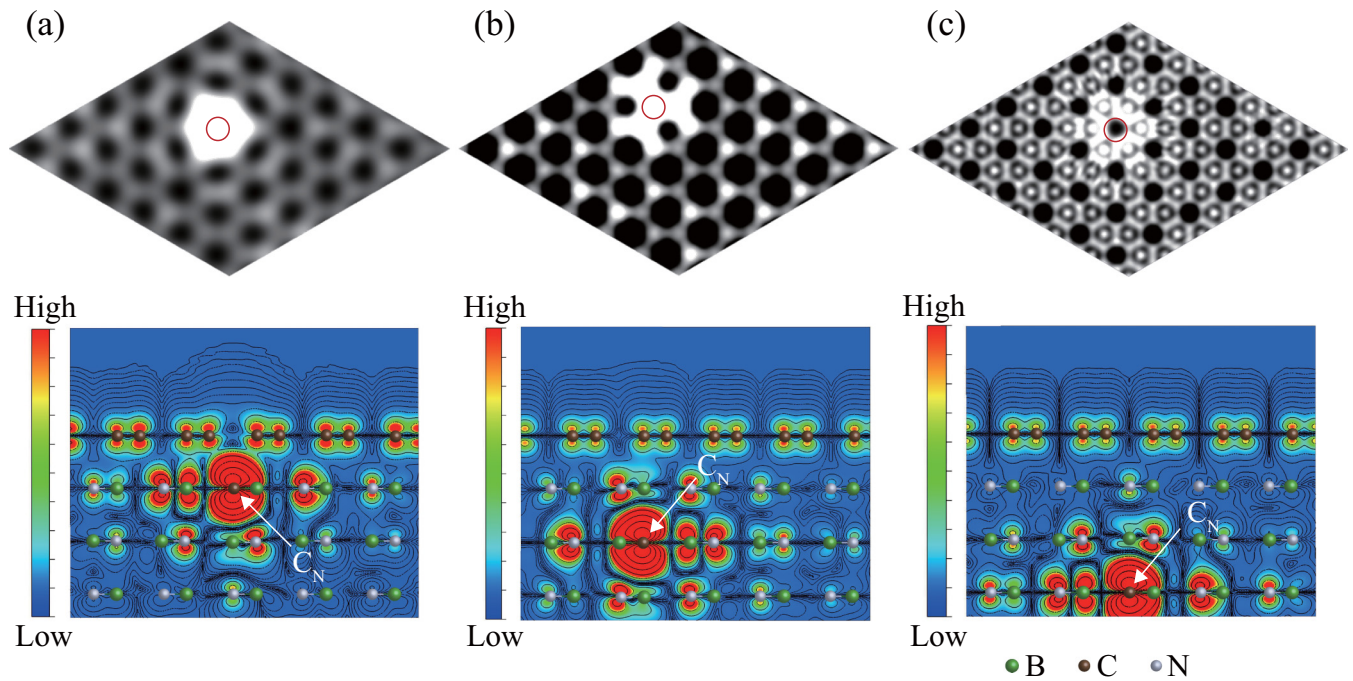
FIG. 10. Simulated STM images (upper panels) and contour maps (lower panels) of $Abb'b$ stacked four-layer systems over the graphene layer stacked on C-doped h-BN at the N site in (a) top layer (1L), (b) middle layer (2L), and (c) bottom layer (3L) of h-BN trilayers. The STM images are constructed at an applied bias voltage of -0.2 eV. The brightness of each image is tuned independently so the contrast around the C_N region becomes clear. On the other hand, contour maps are drawn with the same logarithmic scale for all three maps, indicating clearly that (b) is much brighter than (c), and (a) is also much brighter than (b). The red circles drawn in the bright areas of the STM image denote the position of the C atom doped in the h-BN layers.

N atom is replaced by the larger C atom, it can affect the wider region than the replacement of the B atom by the C atom which is now smaller than the B atom.

We finally study how the STM images of the graphene on the C-doped h-BN trilayer vary depending on the C-doped layer number in the h-BN trilayer. The STM images and the contour maps of the EI-LDOS for the graphene/C-doped h-BN trilayers at the N site in the top layer, the middle layer, and the bottom layer among the h-BN trilayers are shown in Figs. 10(a)–10(c), respectively. In addition to the gradual change of the brightness of the STM images of three cases, the shapes of the bright areas are found to be different from one another. When the C atom is doped in the top h-BN layer, the hexagonlike very bright area above the C impurity in the underlying h-BN emerges in the STM image shown in Fig. 10(a), as in the case of the Ab-stacked two-layer heterostructure of the graphene/C-doped h-BN at the N site shown in Fig. 6(b). In the case of the C atom substitution at the middle h-BN layer, there appears a large bright and complicated area with the threefold rotational symmetry extended around the C impurity in the underlying h-BN in the STM image. Accordingly, the spatial distributions of the EI-LDOS above the C impurity in the h-BN layers are clearly extended to the vacuum region above the graphene layer for C_N dopant in the top and the middle h-BN layer. When the C atom is doped in the bottom h-BN layer, the STM image still has a hexagonlike relatively bright area above the C impurity in the h-BN layer as well. Thus, it is interesting that the STM images may tell the C-doped h-BN layer number. The experimentally reported STM images of the impurity-induced state for the graphene with the h-BN substrate [21] may correspond to the C_N-induced state studied here. Although the experimental impurity density could be less than the present study and therefore the acceptor state should be higher in energy than the present case. The bright spot associated with the acceptor state induced by the C atom doped at the N site in the h-BN layer might correspond to the bright dots mentioned in the experimental study. Furthermore, it has been also reported that there are variations in the intensity of bright dots in the STM experiment [21]. This could mean that the brightness of the dots depends on the depth of the C-doped h-BN layer at the N site, since the acceptor states even in the deep h-BN layer are found to affect the STM images of graphene surface from the graphene surface as discussed above.

IV. SUMMARY

We have investigated the electronic properties and the STM images of the graphene/C-doped h-BN heterostructures using the first-principles calculations based on DFT. It is found that the substitutional doping of the C atom at the B or N site in underlying h-BN layers can give rise to asymmetric effects on the electronic properties of the system. Since the h-BN atomic layers are the 2D semiconductor materials, this asymmetric behavior of the p-type and n-type C doping is of high importance for using h-BN layers in the future nanoelectronics. It is also found that the C-impurity related state appears in the STM images on the constant-height plane over the graphene layer stacked on the C-doped h-BN layers at the N site, while it does not emerge for the B-site doped case. Furthermore, STM images are found to show distinctive properties depending on the C-doped layer number in multilayer h-BN substrates. Thus, the local electronic states induced by C impurities in h-BN layers doped at the N site can be identified by using STM observations. The present paper has clarified the usefulness of the STM technique for detecting the C_N dopant not only at the topmost layer but also at even deeper layers when the graphene is placed on top of the h-BN layers.

[1] K. S. Novoselov, A. K. Geim, S. V. Morozov, D. Jiang, M. I. Katsnelson, I. V. Grigorieva, S. V. Dubonos, and A. A. Firsov, Nature (London) **438**, 197 (2005).

[2] Y.-W. Tan, Y. Zhang, K. Bolotin, Y. Zhao, S. Adam, E. H. Hwang, S. Das Sarma, H. L. Stormer, and P. Kim, Phys. Rev. Lett. **99**, 246803 (2007).

[3] S. V. Morozov, K. S. Novoselov, M. I. Katsnelson, F. Schedin, D. C. Elias, J. A. Jaszczak, and A. K. Geim, Phys. Rev. Lett. **100**, 016602 (2008).

[4] E. K. Sichel, R. E. Miller, M. S. Abrahams, and C. J. Buiocchi, Phys. Rev. B **13**, 4607 (1976).

[5] L. Lindsay and D. A. Broido, Phys. Rev. B **84**, 155421 (2011).

[6] I. Jo, M. T. Pettes, J. Kim, K. Watanabe, T. Taniguchi, Z. Yao, and L. Shi, Nano Lett. **13**, 550 (2013).

[7] Y. Sakai, T. Koretsune, and S. Saito, Phys. Rev. B **83**, 205434 (2011).

[8] Y. Sakai and S. Saito, J. Phys. Soc. Jpn. **81**, 103701 (2012).

[9] A. K. Geim and I. V. Grigorieva, Nature (London) **499**, 419 (2013).

[10] K. S. Novoselov, A. Mishchenko, A. Carvalho, and A. H. Castro Neto, Science **353**, aac9439 (2016).

[11] K. Watanabe, T. Taniguchi, and H. Kanda, Nat. Mater. **3**, 404 (2004).

[12] B. Arnaud, S. Lebègue, P. Rabiller, and M. Alouani, Phys. Rev. Lett. **96**, 026402 (2006).

[13] G. Cassabois, P. Valvin, and B. Gil, Nat. Photonics **10**, 262 (2016).

[14] K. S. Novoselov, A. K. Geim, S. V. Morozov, D. Jiang, Y. Zhang, S. V. Dubonos, I. V. Grigorieva, and A. A. Firsov, Science **306**, 666 (2004).

[15] J.-H. Chen, C. Jang, S. Xiao, M. Ishigami, and M. S. Fuhrer, Nat. Nanotechnol. **3**, 206 (2008).

[16] C. R. Dean, A. F. Young, I. Meric, C. Lee, L. Wang, S. Sorgenfrei, K. Watanabe, T. Taniguchi, P. Kim, K. L. Shepard, and J. Hone, Nat. Nanotechnol. **5**, 722 (2010).

[17] J. Xue, J. Sanchez-Yamagishi, D. Bulmash, P. Jacquod, A. Deshpande, K. Watanabe, T. Taniguchi, P. Jarillo-Herrero, and B. J. LeRoy, Nat. Mater. **10**, 282 (2011).

[18] P. J. Zomer, S. P. Dash, N. Tombros, and B. J. van Wees, Appl. Phys. Lett. **99**, 232104 (2011).

[19] L. Liu, Y. P. Feng, and Z. X. Shen, Phys. Rev. B **68**, 104102 (2003).

[20] X. Zhao, L. Li, and M. Zhao, J. Phys.: Condens. Matter **26**, 095002 (2014).

[21] D. Wong, J. Velasco Jr., L. Ju, J. Lee, S. Kahn, H.-Z. Tsai, C. Germany, T. Taniguchi, K. Watanabe, A. Zettl, F. Wang, and M. F. Crommie, Nat. Nanotechnol. **10**, 949 (2015).

[22] V. L. Solozhenko, A. G. Lazarenko, J.-P. Petitet, and A. V. Kanaev, J. Phys. Chem. Solids **62**, 1331 (2001).

[23] T. Taniguchi and K. Watanabe, J. Cryst. Growth **303**, 525 (2007).

[24] P. Jaffrennou, J. Barjon, J.-S. Lauret, B. Attal-Tretout, F. Ducastelle, and A. Loiseau, J. Appl. Phys. **102**, 116102 (2007).

[25] O. L. Krivanek, M. F. Chisholm, V. Nicolosi, T. J. Pennycook, G. J. Corbin, N. Dellby, M. F. Murfitt, C. S. Own, Z. S. Szilagyi, M. P. Oxley, S. T. Pantelides, and S. J. Pennycook, Nature (London) **464**, 571 (2010).

[26] S. Azevedo, J. R. Kaschny, C. M. C. de Castilho, and F. de Brito Mota, Nanotechnology **18**, 495707 (2007).

[27] S. P. Huber, E. Gullikson, R. W. E. van de Kruijs, F. Bijkerk, and D. Prendergast, Phys. Rev. B **92**, 245310 (2015).

[28] S. A. Tawfik, S. Ali, M. Fronzi, M. Kianinia, T. T. Tran, C. Stampfl, I. Aharonovich, M. Toth, and M. J. Ford, Nanoscale **9**, 13575 (2017).

[29] N. Berseneva, A. Gulans, A. V. Krasheninnikov, and R. M. Nieminen, Phys. Rev. B **87**, 035404 (2013).

[30] Y. Fujimoto and S. Saito, Phys. Rev. B **93**, 045402 (2016).

[31] P. Hohenberg and W. Kohn, Phys. Rev. **136**, B864 (1964).

[32] W. Kohn and L. J. Sham, Phys. Rev. **140**, A1133 (1965).

[33] D. M. Ceperley and B. J. Alder, Phys. Rev. Lett. **45**, 566 (1980).

[34] J. P. Perdew and A. Zunger, Phys. Rev. B **23**, 5048 (1981).

[35] D. Vanderbilt, Phys. Rev. B **41**, 7892 (1990).

[36] Z. Zhang, X. C. Zeng, and W. Guo, J. Am. Chem. Soc. **133**, 14831 (2011).

[37] Y. Sakai, S. Saito, and M. L. Cohen, Phys. Rev. B **89**, 115424 (2014).

[38] S. Hemmatiyan, M. Polini, A. Abanov, A. H. MacDonald, and J. Sinova, Phys. Rev. B **90**, 035433 (2014).

[39] Y. Sakai, S. Saito, and M. L. Cohen, J. Phys. Soc. Jpn. **84**, 121002 (2015).

[40] Y. Fujimoto and S. Saito, Phys. Rev. B **94**, 245427 (2016).

[41] J. P. Perdew, K. Burke, and M. Ernzerhof, Phys. Rev. Lett. **77**, 3865 (1996).

[42] S. Grimme, J. Comp. Chem. **27**, 1787 (2006).

[43] V. Barone, M. Casarin, D. Forrer, M. Pavone, M. Sambi, and A. Vittadini, J. Comp. Chem. **30**, 934 (2009).

[44] P. Giannozzi, S. Baroni, N. Bonini, M. Calandra, R. Car, C. Cavazzoni, D. Ceresoli, G. L. Chiarotti, M. Cococcioni, I. Dabo, A. D. Corso, S. de Gironcoli, S. Fabris, G. Fratesi, R. Gebauer, U. Gerstmann, C. Gougoussis, A. Kokalj, M. Lazzeri, L. Martin-Samos, N. Marzari, F. Mauri, R. Mazzarello, S. Paolini, A. Pasquarello, L. Paulatto, C. Sbraccia, S. Scandolo, G. Sclauzero, A. P. Seitsonen, A. Smogunov, P. Umari, and R. M. Wentzcovitch, J. Phy.: Condens. Matter **21**, 395502 (2009).

[45] J. Tersoff and D. R. Hamann, Phys. Rev. B **31**, 805 (1985).

[46] H. Okada, Y. Fujimoto, K. Endo, K. Hirose, and Y. Mori, Phys. Rev. B **63**, 195324 (2001).

[47] Y. Fujimoto, H. Okada, K. Endo, T. Ono, S. Tsukamoto, and K. Hirose, Mater. Trans. **42**, 2247 (2001).

[48] Y. Fujimoto, H. Okada, K. Inagaki, H. Goto, K. Endo, and K. Hirose, Jpn. J. Appl. Phys. **42**, 5267 (2003).

[49] K. Momma and F. Izumi, J. Appl. Crystallogr. **44**, 1272 (2011).

[50] Y. Fujimoto and S. Saito, Phys. Rev. B **84**, 245446 (2011).

[51] L. Zhao, M. Levendorf, S. Goncher, T. Schiros, L. Pálová, A. Zabet-Khosousi, K. T. Rim, C. Gutiérrez, D. Nordlund, C. Jaye, M. Hybertsen, D. Reichman, G. W. Flynn, J. Park, and A. N. Pasupathy, Nano Lett. **13**, 4659 (2013).

[52] R. S. Pease, Nature (London) **165**, 722 (1950).

[53] G. Constantinescu, A. Kuc, and T. Heine, Phys. Rev. Lett. **111**, 036104 (2013).

[54] G. Giovannetti, P. A. Khomyakov, G. Brocks, P. J. Kelly, and J. van den Brink, Phys. Rev. B **76**, 073103 (2007).

[55] C. Jin, F. Lin, K. Suenaga, and S. Iijima, Phys. Rev. Lett. **102**, 195505 (2009).

[56] L. Zhao, R. He, K. T. Rim, T. Schiros, K. S. Kim, H. Zhou, C. Gutiérrez, S. P. Chockalingam, C. J. Arguello, L. Pálová, D. Nordlund, M. S. Hybertsen, D. R. Reichman, T. F. Heinz, P. Kim, A. Pinczuk, G. W. Flynn, and A. N. Pasupathy, Science **333**, 999 (2011).

[57] Y. Fujimoto and S. Saito, J. Ceram. Soc. Jpn. **123**, 576 (2015).

[58] Y. Fujimoto, T. Koretsune, and S. Saito, J. Ceram. Soc. Jpn. **122**, 346 (2014).

[59] Y. Fujimoto and S. Saito, J. Ceram. Soc. Jpn. **124**, 584 (2016).

[60] Y. Fujimoto and S. Saito, Surf. Sci. **634**, 57 (2015).

[61] Y. Baskin and L. Meyer, Phys. Rev. **100**, 544 (1955).

[62] V. Solozhenko, G. Will, and F. Elf, Solid State Commun. **96**, 1 (1995).

[63] T. Kaneko, M. Koshino, and R. Saito, Phys. Rev. B **95**, 125421 (2017).

[64] I. Deretzis, G. Calogero, G. G. N. Angilella, and A. L. Magna, Europhys. Lett. **107**, 27006 (2014).